GeoScienceWorld
Lithosphere
Volume 2022, Article ID 5216125, 16 pages
https://doi.org/10.2113/2022/5216125

Lithosphere

Research Article

Landslide Susceptibility Mapping along the Anninghe Fault Zone in China using SVM and ACO-PSO-SVM Models

Zhuo Chen,[1,2] Hongfu Zhou,[3] Fei Ye,[1] Bin Liu,[4] and Wenxi Fu[1]

[1]*State Key Laboratory of Hydraulic and Mountain River Engineering, College of Water Resource and Hydropower, Sichuan University, Chengdu 610065, China*
[2]*College of Civil Engineering, Sichuan Agricultural University, Dujiangyan, Sichuan 611830, China*
[3]*Chengdu Center, China Geological Survey, Chengdu 610081, China*
[4]*Sichuan Geological Survey, Chengdu 610081, China*

Correspondence should be addressed to Fei Ye; yefei16scu@163.com

Received 1 November 2021; Accepted 16 June 2022; Published 4 July 2022

Academic Editor: Massimiliano Moscatelli

In the present study, a hybrid machine learning model was designed by integrating ant colony optimization (ACO), particle swarm optimization (PSO), and support vector machine (SVM) algorithms. The model was used to map the landslide susceptibility of the Anninghe fault zone in Sichuan Province, China. Based on this, 12 conditioning factors associated with landslides were considered, namely, altitude, slope angle, cutting depth, slope aspect, relief amplitude, stream power index (SPI), gully density, lithology, rainfall, road density, distance to fault, and peak ground acceleration (PGA). The overall performance of the two resulting models was tested using the receiver operating characteristic (ROC), area under the ROC curve (AUC), Cohen's kappa coefficient, and five statistical evaluation measures. The success rates of the ACO-PSO-SVM model and the SVM model were 0.898 and 0.814, respectively, while the prediction rates of the two models were 0.887 and 0.804, respectively. The results show that the ACO-PSO-SVM model yields better overall performance and accurate results than the SVM model. Therefore, in conclusion, the ACO-PSO-SVM model can be applied as a new promising method for landslide susceptibility mapping in subsequent studies. The results of this study will be useful for land-use planning, hazard prevention, and risk management.

1. Introduction

Landslides are one of the most frequent and destructive geological hazards in mountainous regions and have caused huge losses of life and property ([1, 2] and references therein). The factors leading to slope instability include geologic structure, tectonic activity, lithology, topographic relief, earthquake, rainfall, weathering, climate, and human activity [3–7]. These factors can be classified into two types (i.e., internal and external factors). The evolution of the landslide is dominated by the interaction of internal factors and external factors. The identification of landslide risk is a challenging task for local governments and decision-makers, and it is valuable for evaluating the landslide susceptibility of a region. Landslide susceptibility, which refers to the spatial probability of landslide occurrence in a specific area, is often considered the first stage of landslide hazard management [8–10].

Hitherto, landslide susceptibility mapping methods and techniques have used simple expert knowledge first and then gradually evolved into complicated mathematical procedures. With the increasing emphasis on the application of Geographic Information System (GIS) and soft computing techniques, many approaches to landslide susceptibility mapping (LSM) have been adopted around the world in the last four decades. These approaches can be mainly classified into three groups, namely, deterministic, statistical, and machine learning techniques [11]. Deterministic methods incorporate mathematical models of the physical mechanisms controlling slope failure [12], and these methods usually generate accurate results because of their

site-specific and data dependency nature. The factor of safety is generally used as the index of stability by taking into account stabilizing and destabilizing factors. Deterministic methods do not require landslide inventories and are most suitable for a single landslide and a small-scale area. Although reliable geotechnical and hydrogeological data are essential for such methods, the lack of detailed information throughout large-scale areas and the expensiveness remain the main obstacles in the deterministic models.

Due to the challenges of deterministic method application, e.g., the data requirement, cost and infeasibility for large areas, statistical methods are widely used in LSM because they can effectively analyze the functional relationship between past landslides and inferred contributing factors, such as entropy index [13], frequency ratio [14], evidential belief function [15], weight of evidence [16], and logistic regression [17]. However, it should be noted that these methods have a weak ability to assess the nonlinear relationship between landslide occurrence and conditioning factors. To overcome the limitations of statistical methods, machine learning methods have been introduced for landslide susceptibility analysis. Machine learning methods, such as artificial neural networks (ANN) [18], support vector machines (SVM) [19], random forests (RF) [20], adaptive neuro-fuzzy inference system (ANFIS) [21], and Naïve Bayes (NB) [22], provide promising and effective ways to solve complex and nonlinear problems with high accuracy. Nevertheless, some problems still exist with machine learning methods, mainly including the problem of overfitting, parameter optimization, and the improvement of generalization ability.

Literature review shows that SVM has received increasing attention in recent years because of its good classification performance and capabilities of fault tolerance [23]. SVM can obtain good predictions with a limited number of training samples [24], but its parameters need to be carefully selected by a cross-validation method or another optimization technique. A search for optimal parameters in an SVM model plays a crucial role in building a landslide prediction model. To develop an efficient SVM model, kernel function and penalty parameters must be carefully predetermined. Recently, various optimization algorithms, such as genetic algorithms (GA), particle swarm optimization (PSO), ant colony optimization (ACO), and gray wolf optimizer (GWO), have been integrated with machine learning methods to rapidly search for the optimal predetermined parameters [25–27]. Despite all the advantages of these algorithms, they suffer from some problems such as slow convergence and being stuck in a local minimum. To overcome these problems, researchers recently suggested hybrid models [28, 29]. Hybrid techniques provide an effective solution when single models are unable to simultaneously meet multiple needs. A review of methodologies suggests that hybrid models offer higher generalization ability than single models by reducing variance and bias or improving prediction accuracy [30, 31]. However, to date, there are no accepted results on whether a single hybrid model or a group of models is best suited for all case scenarios. Therefore, new hybrid models for LSM should be further explored.

A significant issue in improving SVM predictive accuracy is the need to identify a novel algorithm to optimize the parameter combination. PSO is a population-based stochastic optimization algorithm and has stable convergence characteristics with good computational efficiency. However, PSO suffers from a condition that causes it to converge to a local solution prematurely which happens due to the inability of particles to escape from a local minimum and thus stagnate in those regions. ACO, a new biological evolution simulating method, has the advantages of parallel computing, positive feedback search, and high convergence speed and can be used to overcome the limitations of PSO. In this study, a new hybrid method was built on the support of the ACO and PSO algorithms to optimize the penalty parameter and the kernel function. The new method can improve the predictive performance of the SVM model and produce highly reliable susceptibility maps. Additionally, the Anninghe fault zone was selected as the study area due to the frequent landslide hazard in this area. The results and conclusions obtained in this paper have implications for landslide prevention in the study area and other relevant research.

2. Study Area

The study area is located on the eastern margin of the Tibetan Plateau, geographically between longitudes 101°59′ E and 102°23′E and latitudes 27°50′N and 29°28′N (Figure 1). The study area mostly consists of mountainous landforms (land slope ranging from 0 to 85°), with the highest and lowest altitudes of 5,531 m and 811 m, respectively. The study area has a subtropical monsoon climate with an average annual temperature of 15°C. According to local meteorological organizations, the average annual rainfall is over 1,000 mm, and the rainy season is from May to October [32]. The study area belongs to the eastern segment of the Sichuan-Yunnan rhombic block, where active faults are well developed. Historical documents show that earthquakes of surface wave magnitude (Ms) ≥ 5.0 (such as the 1489 Ms 6.75 Zimakua earthquake, the 1977 Ms 5.3 Lugu earthquake, and the 1985 Ms 6.0 Mianning earthquake) often occur along the Anninghe fault [32]. The Anninghe fault zone is generally considered one of the regions in southwestern China with the most developed, active, and extensive distribution of landslides. According to the Emergency Management Office of Sichuan Province, many people are living under the potential threat of landslides in the study area. Therefore, it is highly necessary to conduct a landslide prediction analysis in the Anninghe fault zone, which could help local government and decision-makers take necessary actions to bring harmony between economic development and the environment. The occurrence of landslides is controlled by various factors such as topographical features, lithology and tectonics, climate, human interference, and natural environment [33–35]. The relationships between landslide conditioning factors and landslide occurrence generally vary by location, making it difficult to confirm which environmental factors are the most important and necessary among them.

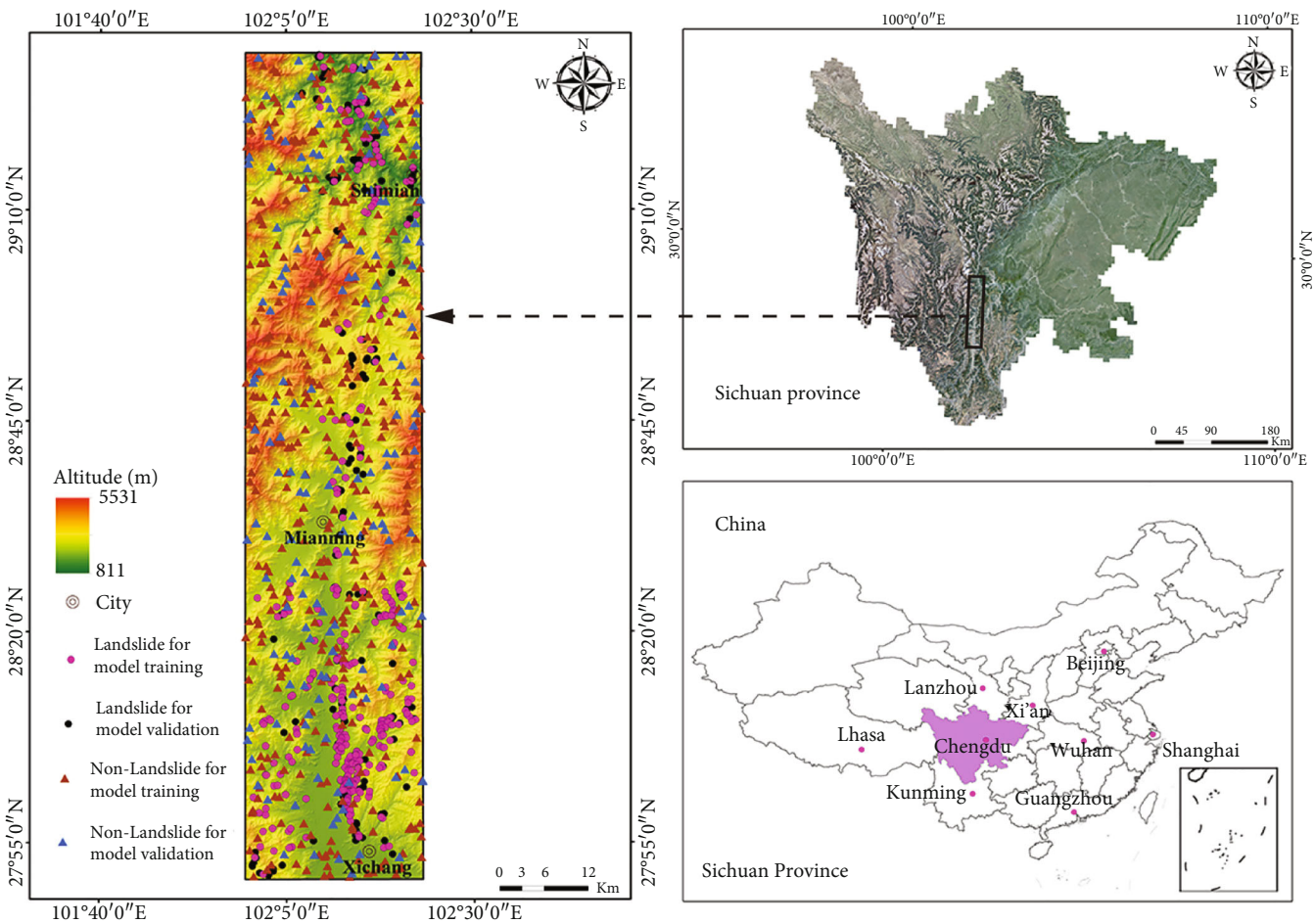

Figure 1: Location of the study area.

3. Materials

3.1. Landslide Conditioning Factors. A number of conditioning factors previously employed in the literature were examined to produce the LSM. Nevertheless, the selection of suitable factors is a key step for LSM, as factor selection affects the predictive capabilities of numerous models. Currently, there are no standard guidelines or clear protocols regarding the selection of conditioning factors [19, 36]. According to the geo-environmental conditions, availability of data sources, and analysis of landslide genesis mechanisms, twelve conditioning factors including altitude, slope angle, slope aspect, relief amplitude, cutting depth, gully density, stream power index (SPI), lithology (Table 1), rainfall, road density, distance to faults, and peak ground acceleration (PGA) (Figure 2) were selected. All thematic layers were prepared in a raster format with a 30 m spatial resolution.

Altitude, controlled by several geological and geomorphological processes, is frequently used in most LSM research [37]. Altitude was grouped into five classes: <1,868 m, 1,868–2,407 m, 2,407–2,978 m, 2,978–3,670 m, and>3,670 m (Figure 2(a)).

Slope angle is an indispensable influencing factor in LSM, and it is directly related to the shear stresses acting on the displacement of hill slopes [38]. Slope angle in the study area was reclassified into nine categories: <10°, 10–15°, 15–20°, 20–25°, 25–30°, 30–35°, 35–40°, 40–45°, and>45° (Figure 2(b)).

Slope aspect determines the degree of solar radiation on the slope surface, which can influence the soil moisture and slope stability [26]. As shown in Figure 2(c), the slope aspect was categorized into nine directional classes, including eight directions and flat.

Relief amplitude refers to the difference between the altitude of the highest point and the altitude of the lowest point in a particular area and can effectively reflect the gravitational potential energy of terrain that is closely related to landslide occurrence [39]. In this study, the relief amplitude was reclassified into five classes: <103 m, 103–191 m, 191–268 m, 268–358 m, and>358 m (Figure 2(d)).

Cutting depth is the difference between the average elevation and lowest elevation in a determined area and is an important parameter in LSM [1]. Cutting depth was divided into five categories: <50 m, 50–97 m, 97–142 m, 142–192 m, and >192 m (Figure 2(e)).

Gully density, defined as the channel length per unit area, represents an effective factor in LSM [1]. Gully density of the study area was classified into six classes: <0.47 km/km^2, 0.47–0.82 km/km^2, 0.82–1.14 km/km^2, 1.14–1.50 km/km^2, 1.50–1.95 km/km^2, and >1.95 km/km^2 (Figure 2(f)).

Table 1: Description of the geological units.

Group	Code	Lithology	Geological age
Group 1	Qad^{1-3}, Qal, Qh, Qp, Qgl	Gravel, sand, loam, sandy silt, clay	Quaternary
Group 2	N_2x	Conglomerate, sandy conglomerate, shale	Neogene
Group 3	K_1x^1, K_1x^2	Calcareous siltstone, feldspathic quartz-sandstone, conglomerate, mudstone, marl	Cretaceous
Group 4	J_3f, J_2g, J_2x, J_2y, J_2n, Jxk, Jxg, xε1 5, εo1 5, xr1 5, εx1 5, ro1 5, $T_{1\text{-}2}$, δo1 5, r2 5, rk1 5, δ1 5, rσ2 4, T_3x	Mudstone, calcareous fine sandstone, conglomerate, marl, feldspathic quartz-sandstone, siltstone, shale, syenite, granite, porphyry, phyllite, slate, diorite, schist, dolomite	Jurassic-Triassic
Group 5	P_1, P_1q+m, P1 1, P2 1, P3 1, P_2, $P_2\beta$, P3 2, P4 2, P2 3, V3 4, N3 4, $\beta\mu$3 4	Limestone, basalt, gabbro, diabase, marble, slate, phyllite, metamorphic sandstone, quartzite	Permian
Group 6	D1 2, D_2h, D_2b, D_2z, D2 3, $AnD_2\lambda$	Slate, phyllite, limestone, marble, metamorphic sandstone, dolomite	Devonian
Group 7	$Z_a\lambda$, Z_ak, Z_bd, Z_as, r_2, V2 2, ε2 2, Z_bg, δ_2, Za^a	Rhyolite, porphyry, tuff, dolomite, limestone, calcareous shale, marl, sandstone, sandy conglomerate, basalt, granite, gabbro, diorite	Sinian System
Group 8	Pt_1l^3, Pt_1l^2, Pt_1l^1, Pt_1tn, Pt_1f, Pt_1	Phyllite, marble, sandstone, quartzite, slate, dolomite, limestone	Pre-Sinian System

The SPI reflects the intensity of stream erosion on the surface and therefore influences the occurrence of landslides [39]. The SPI values were divided into six classes: <6, 6–12, 12–18, 18–24, 24–30, and >30 (Figure 2(g)).

Lithology is a key factor for LSM, and some geological formations are more favorable to landslides [28]. There are eight main lithological groups in the study area (Figure 2(h) and Table 1).

Rainfall is an important factor for landslides, especially in mountainous areas [19]. The occurrence of a landslide is influenced by the intensity and durability of rainfall. In this study, the maximum 24 h rainfall was used to map landslide susceptibility (Figure 2(i)).

Road density presents the relationship between human activities and landslide occurrence, and it affects the slope stability [40]. Road density was divided into nine classes: <0.19 km/km^2, 0.19–0.65 km/km^2, 0.65–1.19 km/km^2, 1.19–1.81 km/km^2, 1.81–2.65 km/km^2, 2.65–3.81 km/km^2, 3.81–5.31 km/km^2, 5.31–7.31 km/km^2, and >7.31 km/km^2 (Figure 2(j)).

The shearing strength of the slope rock mass is reduced due to the presence of faults [14]. Distance to faults represents the degree of rock fracture. Distance to faults was divided into eight classes: <300 m, 300–600 m, 600–900 m, 900–1200 m, 1200–1500 m, 1500–1800 m, 1800–2100 m, and >2100 m (Figure 2(k)).

PGA is considered an important dynamic factor that measures the impact of earthquakes on landslides [41]. In the study area, it was observed that most landslides took place in areas with PGA greater than 0.2, indicating the significant influence of earthquakes on landslide disasters.

3.2. Landslide Inventory. The preparation of a landslide inventory map is essential for studying the spatial relationships between historical landslide distributions and their conditioning factors. In the present study, a series of base maps were collected, including a 30 m resolution digital elevation model (DEM), multisource high-resolution satellite images, geological maps, river maps, rainfall maps, and road maps. The primary data source information is shown in Table 2. The landslide inventory map of the Anninghe fault zone was produced through extensive field surveys, historical landslide records, and visual interpretation of satellite imagery. In this study, the landslide information was obtained from a preexisting multitemporal landslide inventory prepared at 1 : 50,000 scale through the systematic visual interpretation of ten stereoscopic, panchromatic, and multispectral satellite image pairs acquired in August 2004, March 2006, May 2010, April 2011, June 2013, May 2014, August 2015, April 2016, January 2017, and February 2019. Furthermore, the landslide information was supplemented by field checks and surveys executed in various periods from 2014 to 2016, in July 2017, and in August 2018. A total of 547 landslides were detected and mapped in the study area (Figures 1 and 3). The geometry of a landslide is best represented by a polygon in vector format. In this study, the entire scarp polygon was used for the landslide sampling strategy. A total of 383 landslides (70%) were randomly chosen for model construction, and the remaining 164 landslides (30%) were used for model validation. In addition, the same number of nonlandslide locations was randomly generated from areas less susceptible to landslides.

4. Methods

4.1. Landslide Conditioning Factor Selection based on the Information Gain Ratio (IGR). The quality of LSM depends on both the selected models and the predictive capability of the conditioning factors. Since not all landslide conditioning factors have the same predictive capability in LSM, several factors may sometimes generate severe interference, which reduces the overall predictive capability of the employed models. Therefore, conditioning factors with low or null predictive capability should be removed to obtain more accurate results. There are several methods for selecting features in the literature review, such as genetic

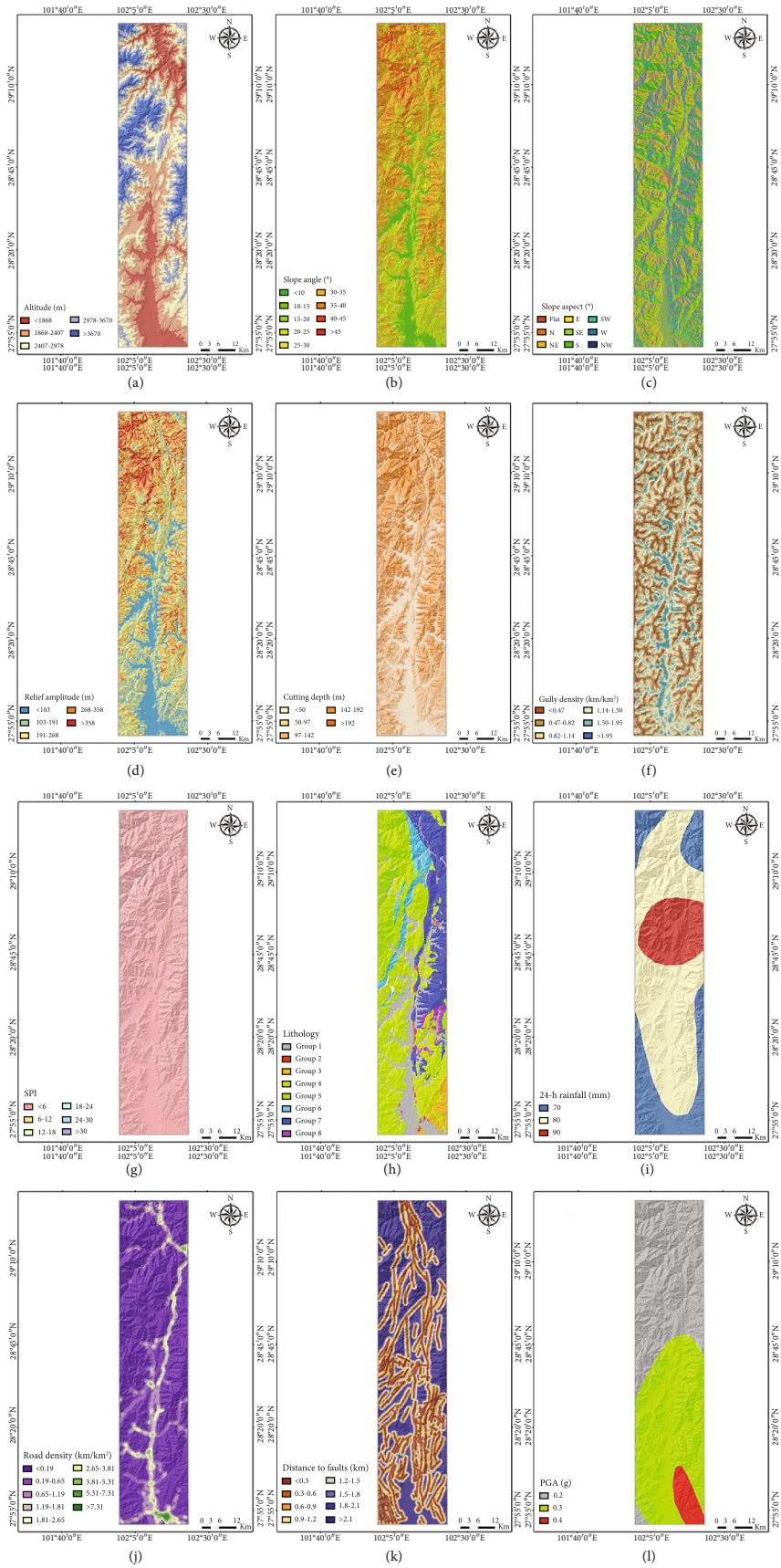

Figure 2: Landslide conditioning factor maps: (a) elevation; (b) slope angle; (c) slope aspect; (d) relief amplitude; (e) cutting depth; (f) gully density; (g) SPI; (h) lithology; (i) 24 h rainfall; (j) road density; (k) distance to faults; (l) PGA.

Table 2: Data used in spatial modeling for LSM.

Dataset	Factors	Scale/resolution	Primary format	Data source
Landslide inventory	Altitude		Vector	China Geological Survey
DEM	Slope angle	30 m	Grid	ASTER satellite
Geological map	Slope aspect	1 : 200,000	Vector	China Geological Survey
Road	Relief amplitude	1 : 10,000	Vector	China Geological Survey
Rainfall	Cutting depth	30 m	Grid	China Geological Survey
Rivers	SPI	1 : 10,000	Vector	China Geological Survey
Gaofen-1 image	Lithology	2 m	Grid	Chinese satellite Gaofen-1
Gaofen-2 image	Rainfall	1 m	Grid	Chinese satellite Gaofen-2
WorldView-2 image	Road density	0.5 m	Grid	DigitalGlobe
WorldView-3 image	Distance to faults	0.31 m	Grid	DigitalGlobe
SPOT-6 image	PGA	1.5 m	Grid	Astrium
Google Earth image	Gully density	0.61 m	Grid	Google Earth

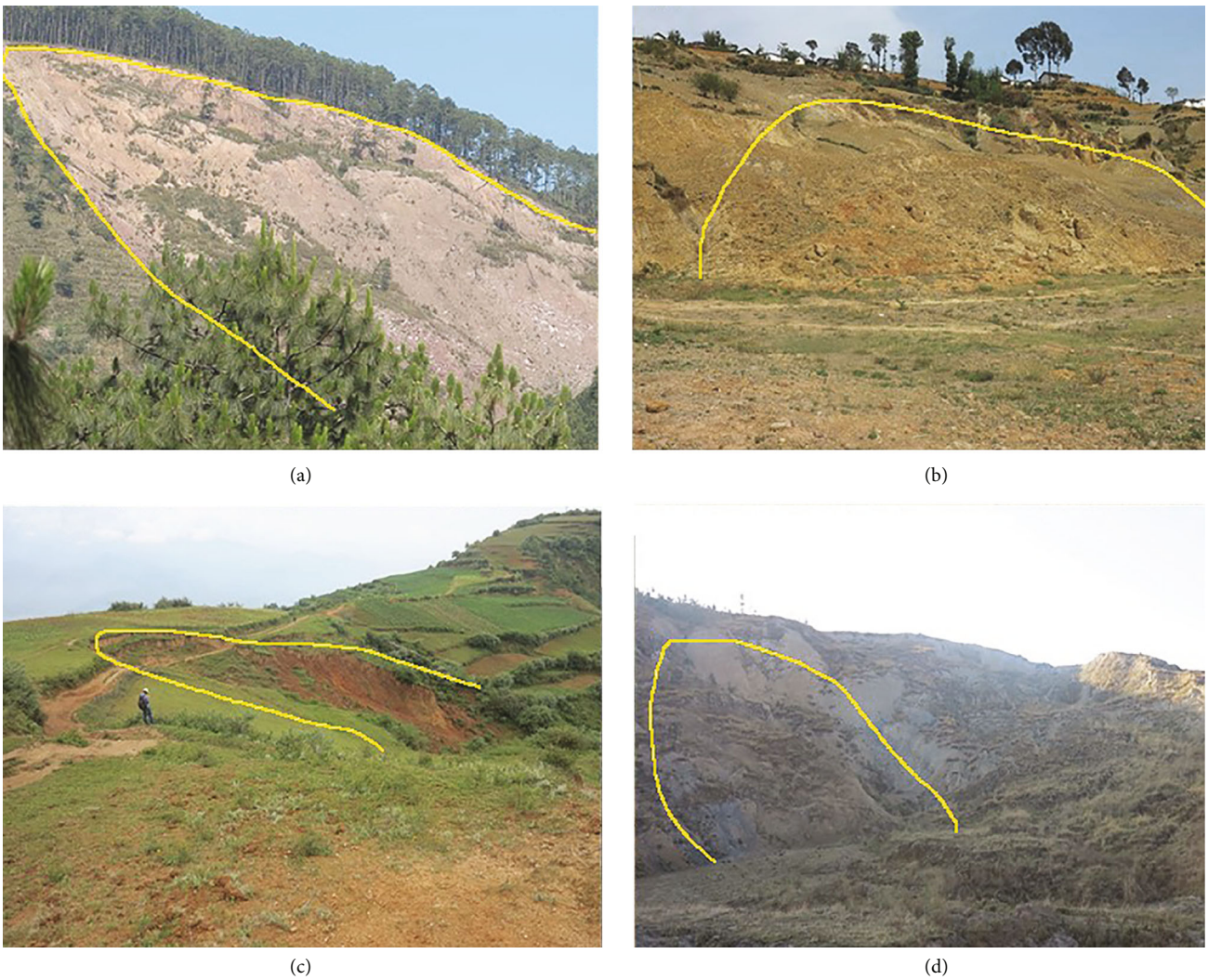

Figure 3: Field photographs of some typical landslides.

algorithms [42], chi-square statistic [43], information gain ratio [44], and linear support vector machine [45]. In this study, the information gain ratio (IGR) was chosen to evaluate the predictive capability of the twelve landslide conditioning factors. Assuming that a training data T consists of n input samples and belongs to the class label Y_i (presence

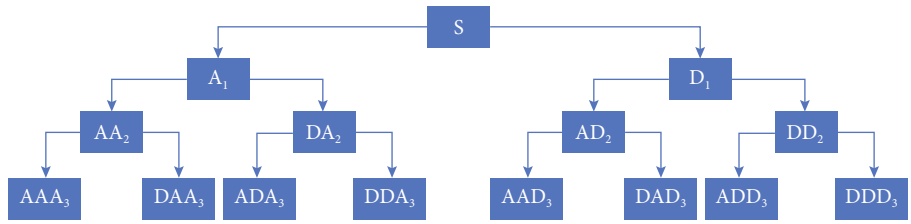

Figure 4: The structure diagram of the three-level wavelet packet decomposition tree.

and absence of landslide), then the IGR of the landslide causal factors C and T can be calculated as

$$\mathrm{Info}(T) = -\sum_{i=1}^{2} \frac{n(Y_i, T)}{|T|} \log_2 \frac{n(Y_i, T)}{|T|}, \tag{1}$$

$$\mathrm{Info}(T, C) = \sum_{j=1}^{m} \frac{T_j}{|T|} \mathrm{Info}(T), \tag{2}$$

$$\mathrm{IGR}(T, C) = \frac{\mathrm{Info}(T) - \mathrm{Info}(T, C)}{\mathrm{SplitInfo}(T, C)}, \tag{3}$$

$$\mathrm{SplitInfo}(T, C) = -\sum_{j=1}^{m} \frac{|T_j|}{|T|} \log_2 \frac{|T_j|}{|T|}. \tag{4}$$

4.2. Wavelet Packet Transform (WPT). The wavelet transform, as a robust signal processing approach, is similar to the Fourier transform with a completely different merit function and can produce both time and frequency information [46]. The wavelet transform provides a useful decomposition of the original signal and enhances the predictive capability of the employed models by capturing useful information at various levels. Wavelet transforms can be summarized into two types: continuous wavelet transforms (CWTs) and discrete wavelet transforms (DWTs). The CWT requires a substantial amount of redundant information to be processed and entails a high computational cost. In contrast, DWT requires less computation time and data, making it suitable for online applications. However, DWT presents substantial limitations in offering an in-depth analysis of high-frequency signal components. To improve the analysis of high-frequency components, the wavelet packet transform (WPT) was used to generate more frequency bands, which enhanced the ability to extract relevant information from the original signal. The WPT is a generalization of the wavelet transform and provides a richer analysis of the signal. Figure 4 shows the three-level wavelet packet decomposition tree of the original signal. The original signal (S) was decomposed into approximation (A) and detail (D). This procedure was iteratively performed at different levels.

4.3. Ant Colony Optimization (ACO). Ant colony optimization (ACO), as a kind of simulative evolutionary algorithm, is inspired by the foraging behavior of ants in nature [47]. Ants can find the shortest route between the food source and their nest. Indirect communication skills between ants are the cooperative behavior of ants based on pheromone trails. Routes with a large amount of pheromones are most often chosen by ants. Therefore, the shortest route is considered the optimal solution to an optimization problem. The three main phases of ACO are solution construction, pheromone update, and daemon action. The process of solution construction and pheromone update is repeated for several iterations until the termination criteria are reached. The daemon action is an optional step in ACO, which involves applying other updates from a global perspective.

4.4. Particle Swarm Optimization (PSO). Particle swarm optimization (PSO) is a powerful population-based optimization approach that is grounded in the social behavior of birds flocking in the real world. PSO is widely used in solving the global optimal solution of large-scale nonlinear problems [48]. Each member in PSO is identified as a particle and points to a solution in the search space. The PSO can search for the optimal solution from several initial solutions using iterative computation. Through the PSO performance, the global best of particles and the personal best of particles are recorded as g_{best} and p_{best}, respectively. Each particle constantly updates itself through p_{best} and g_{best} to create a new population.

4.5. Support Vector Machine (SVM). Support vector machine (SVM) is a supervised machine learning method, which can be used for both classification and regression [49]. In recent years, SVMs have received a lot of attention due to their good classification performance and fault tolerance capabilities. Owing to its complex structure, even nonlinearly separable cases can be handled using this method. The main goal of SVMs is to find the optimal hyperplane between two classes of the training dataset (Figure 5). The optimal hyperplane can be determined by minimizing the following objective function [50]:

$$\mathrm{Min} \sum_{i=1}^{n} \alpha_i - \frac{1}{2} \sum_{i=1}^{n} \sum_{j=1}^{n} \alpha_i \alpha_j y_i y_j (x_i, x_j), \tag{5}$$

subject to the following constraint:

$$\mathrm{Min} \sum_{i=1}^{n} \alpha_i y_j = 0, 0 \le \alpha_i \le C, \tag{6}$$

where α_i are the Lagrange multipliers and C is the penalty. The decision function can be given as follows:

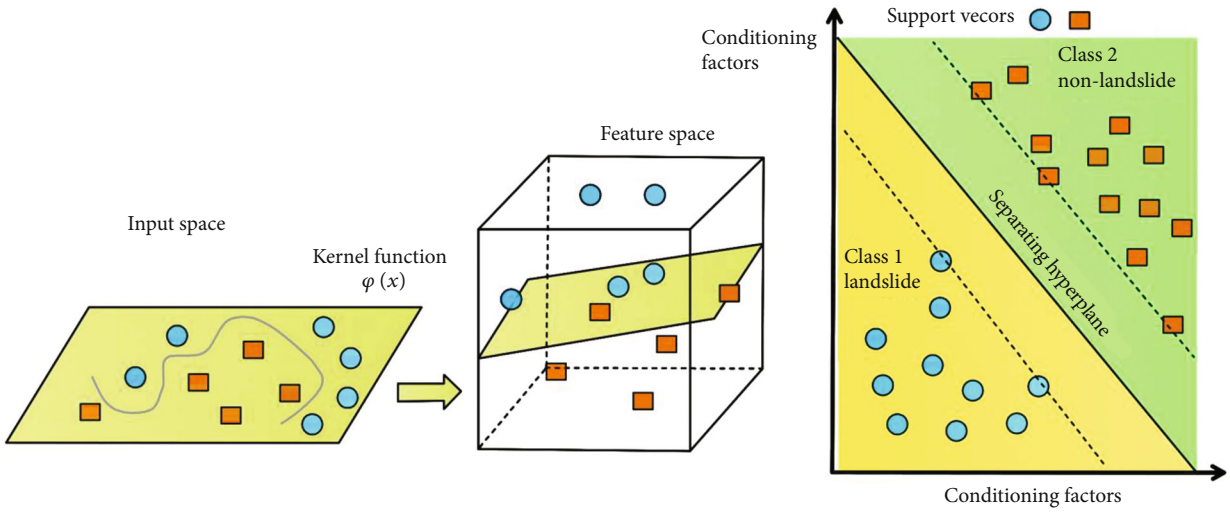

Figure 5: Illustration of the SVM principle.

$$g(x) = \operatorname{sgn}\left(\sum_{i=1}^{n} y_i a_i K(x_i, x_j) + b\right), \tag{7}$$

where $K(x_i, x_j)$ is the kernel function.

4.6. Combination of ACO-PSO-SVM. In this study, a hybrid model based on ACO, PSO, and SVM algorithms is proposed to improve the solution performance of single models. The SVM was chosen as the base classifier to construct the hybrid ACO-PSO-SVM model for evaluating landslide susceptibility. Figure 6 shows the training and learning process in the hybrid ACO-PSO-SVM model. The ACO-PSO-SVM model consists of the following steps:

(1) Decompose the base maps (i.e., landslide conditioning factor maps) into approximation and detail components, and use them with minimum entropy values as inputs

(2) Initialize the parameters of ACO and update the pheromones. The selection of the jth point, where an ant at the ith point in iteration t will go, is based on

$$P_{ij}^{k} = \begin{cases} \dfrac{[\tau_{ij}(t)]^{\alpha}[\eta_{ij}]^{\beta}}{\sum[\tau_{ij}(t)]^{\alpha}[\eta_{ij}]^{\beta}}, & \text{if } j \text{ is allowed point,} \\ 0, & \text{otherwise,} \end{cases} \tag{8}$$

where P_{ij} is the transition probability, τ_{ij} is the amount of pheromones between points i and j, η_{ij} is the reciprocal of d_{ij}, d_{ij} is the distance between the ants, and α and β are two weight factors.

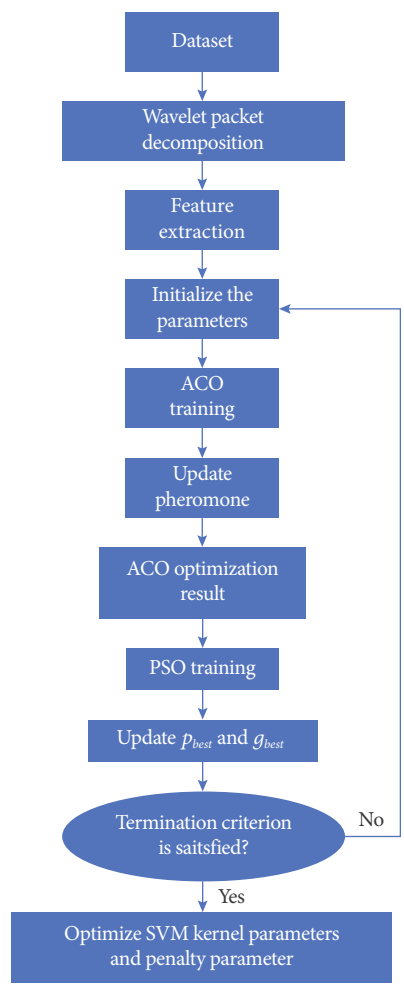

Figure 6: The flowchart of the proposed ACO-PSO-SVM model.

The pheromone routes are updated using the following equations:

$$\tau_{ij}(t+1) = (1-\rho)\tau_{ij}(t) + \Delta\tau_{ij}^{k}(t, t+1), \tag{9}$$

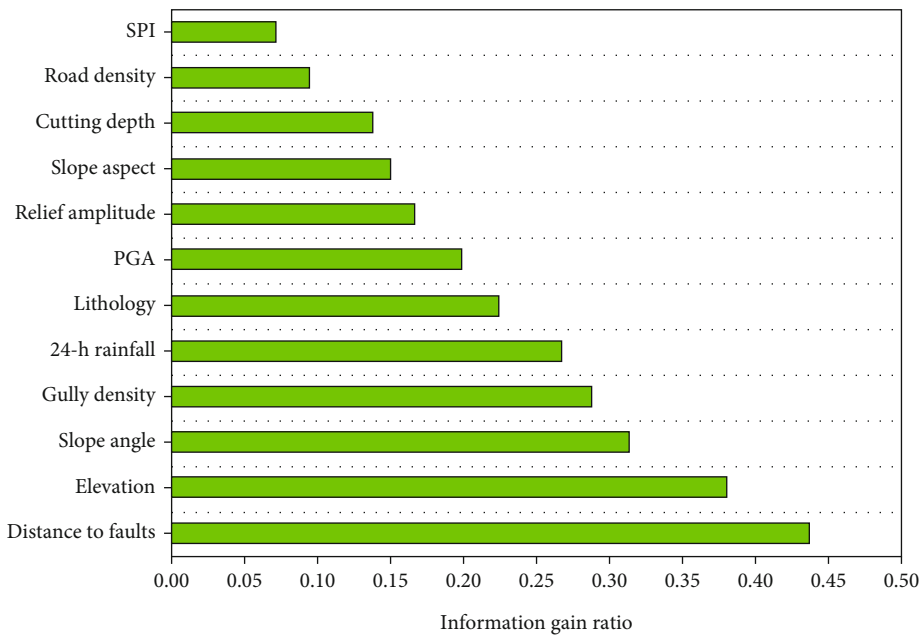

Figure 7: Predictive power of the twelve landslide conditioning factors.

$$\Delta\tau_{ij}^{k}(t, t+1) = \sum_{k=1}^{n} \Delta\tau_{ij}^{k}(t, t+1), \tag{10}$$

where ρ is the evaporation coefficient and receives a value at the interval [0–1].

(3) Initialize the parameters of the PSO and update the velocity and position of each particle. Equations (11) and (12) demonstrate the position and velocity of the particles, respectively

$$V_2 = \omega V_1 + C_1 r_1 (p_{\text{best}} - X_1) + C_2 r_2 (g_{\text{best}} - X_1), \tag{11}$$

$$X_2 = X_1 + V_2, \tag{12}$$

where V_1, V_2, X_1, and X_2 represent the current and new velocities and positions of each particle, respectively; ω is the inertia weight; C_1 and C_2 are the positive acceleration constants; r_1 and r_2 are random numbers in the range [0, 1].

(4) For each particle, if $p_{\text{best}} > g_{\text{best}}$, then g_{best} will be replaced by p_{best}. Stop the iterative process if the termination criteria are met; otherwise, return to step 2 to continue the process

(5) Optimize the SVM kernel parameters and penalty parameters to obtain the final classification results

4.7. Performance Measures. To evaluate and compare the performance of the models, statistical index-based methods including positive predictive value (PPV), negative predictive value (NPV), sensitivity (SST), specificity (SPF), accuracy (ACC), and Cohen's kappa coefficient (κ) were used. These statistical indices are calculated based on the confusion matrixes resulting from the SVM and ACO-PSO-SVM models. Another way to measure the classification performance of the models is to use the ROC curve. It is created by plotting sensitivity against 100-specificity based on a series of different dichotomies. The AUC represents the statistical reliability of the models. The AUC value ranges from 0 to 1, where an AUC value closer to 1 corresponds to better model performance.

5. Results

5.1. Relative Importance Analysis of Landslide Conditioning Factors. The predictive capability of the twelve landslide conditioning factors was evaluated using a training set based on the IGR approach. The conditioning factors with higher IGR values represent higher predictive power in the LSM and vice versa. The predictive capability of all conditioning factors using the IGR approach is shown in Figure 7. The results indicate that distance to faults is the most important factor for landslide prediction, followed by altitude, slope angle, gully density, rainfall, lithology, PGA, relief amplitude, slope aspect, cutting depth, road density, and SPI. In the current study, the IGR values of all factors were greater than zero, indicating that these factors contribute to the predictive capability of landslide susceptibility modeling. Therefore, they are suitable for further analysis.

5.2. Generation of Landslide Susceptibility Maps. Landslide susceptibility maps for both models were generated using ArcGIS software and are shown in Figures 8 and 9. To identify distinctions in LSM across the study area, both landslide susceptibility maps were reclassified into five classes: very low (<0.116), low (0.116-0.296), moderate (0.296-0.535), high (0.535-0.784), and very high (>0.784). The two models produced similar landslide susceptibility results. The very high and high susceptibility areas are distributed mainly in the middle and southern parts of the study area, which

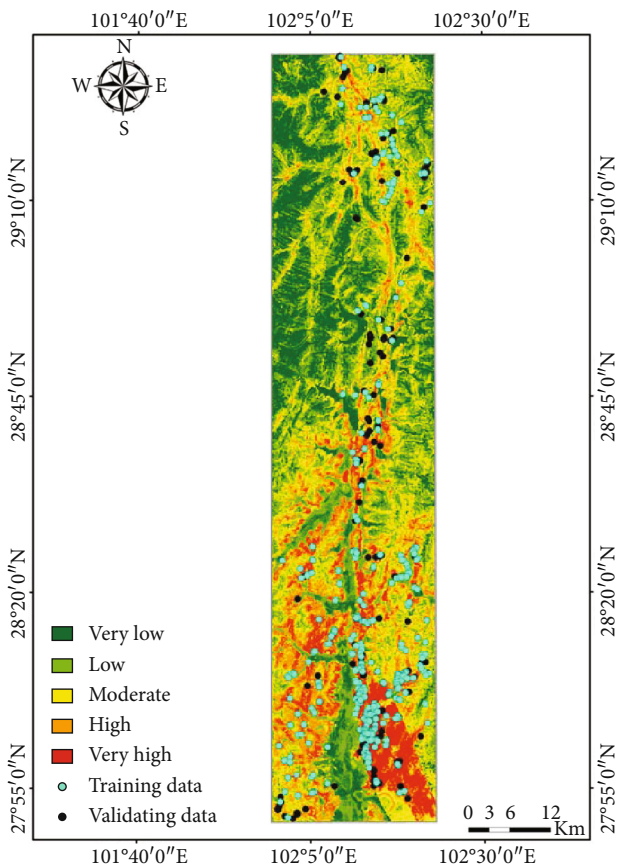

Figure 8: Landslide susceptibility map produced by the SVM model.

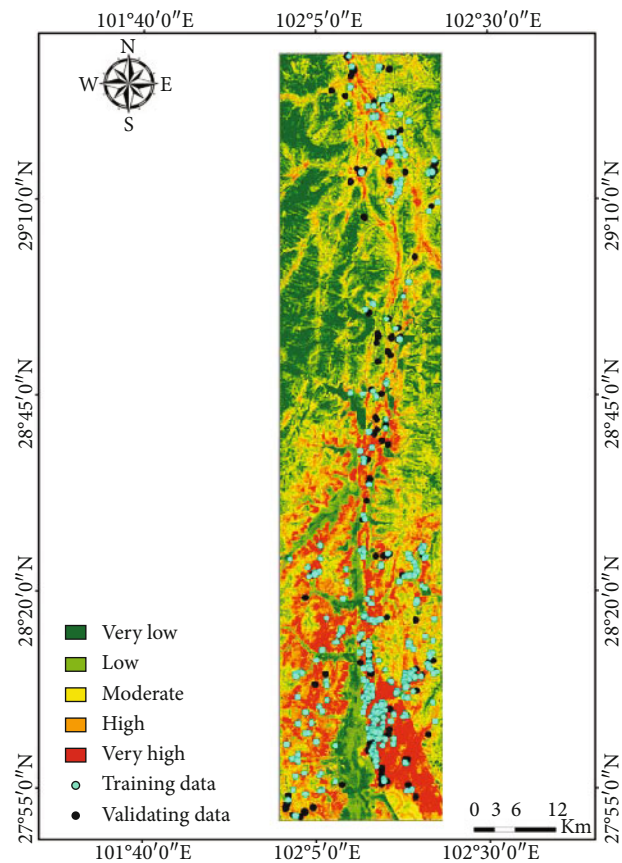

Figure 9: Landslide susceptibility map produced by the ACO-PSO-SVM model.

correspond to areas of distance to faults (<1.2 km) and altitude (<2407 m). The joints and fractures of the slope rock mass near the fault zone are well developed and have poor mechanical properties, which reduce the stability of the slope. Compared with high-altitude areas, landslides are more likely to occur in low altitude areas. Engineering construction and cultivation are mainly concentrated in these areas and contribute to the occurrence of landslides. The very low and low susceptibility areas are mainly located in the northwestern part of the study area, with high altitudes and high slopes, and these variables are unsuitable for the development of landslides.

5.3. Model Performance and Validation. The performances of the modeling process using PPV, NPV, SST, SPF, ACC, and κ during the training and validation phases are shown in Tables 3 and 4. Regarding the training dataset, the statistical index metrics for the ACO-PSO-SVM model have the best performance. The kappa indices for the SVM and ACO-PSO-SVM models are 0.559 and 0.756, respectively, indicating a substantial agreement between the observed and predicted landslides. The results of the validation dataset have the same pattern compared to the training dataset. Using ROC curve analysis, the general performance of the two models on both training and validation datasets is shown in Tables 5 and 6 and Figure 10. For the training dataset, the ACO-PSO-SVM model has an AUC value of 0.898, which is higher than that of the SVM (0.814) model. Regarding the validation dataset, the ACO-PSO-SVM model has an AUC value greater than 0.887. The results indicate that the ACO-PSO-SVM model has better predictive power than the SVM model.

Table 3: Model performance on the training dataset.

Models	PPV	NPV	SST	SPF	ACC	κ
SVM	0.790	0.766	0.771	0.785	0.778	0.559
ACO-PSO-SVM	0.880	0.829	0.835	0.876	0.854	0.756

Table 4: Model performance on the validation dataset.

Models	PPV	NPV	SST	SPF	ACC	κ
SVM	0.783	0.747	0.755	0.775	0.765	0.541
ACO-PSO-SVM	0.862	0.826	0.831	0.858	0.844	0.743

Table 5: AUC analysis for the two landslide models with the training dataset.

Models	AUC	SE	95% CI
SVM	0.814	0.0261	0.761-0.859
ACO-PSO-SVM	0.898	0.0187	0.855-0.932

Table 6: AUC analysis for the two landslide models with the validation dataset.

Models	AUC	SE	95% CI
SVM	0.804	0.0267	0.750-0.850
ACO-PSO-SVM	0.887	0.0200	0.842-0.923

By comparing SE and 95% CI, the ACO-PSO-SVM model has the smallest SE (0.0187) and the narrowest 95% CI (0.855–0.932), followed by the SVM model (SE = 0.0261 ; 95%CI = 0.761–0.859). The training datasets of the two models all produce reasonable goodness of fit, and the model with the best performance between the two models is the ACO-PSO-SVM model. The results of the established landslide model were verified with the validation dataset, and the results are shown in Table 6. The ACO-PSO-SVM model still exhibits the smallest SE (0.0200) and the narrowest 95% CI (0.842–0.923). Because the two evaluation indices of the ACO-PSO-SVM model are better than those of the SVM model, the ACO-PSO-SVM model performs the best with the validation dataset. The difference is that the areas with very high and high susceptibility in the maps obtained by the ACO-PSO-SVM model are larger than those produced by the SVM model, and the SVM model shows lower prediction accuracy in these areas.

In addition, the results show that the ensemble model has greater classification accuracy than the SVM model. The ACO-PSO-SVM model showed superior performance in accurately classifying low- and very low-susceptibility regions, and high- and very high-susceptibility areas. Although the proximity of AUC values of the SVM model and the ACO-PSO-SVM model could imply marginal differences in model performance, the resulting maps show that the SVM model is prone to misclassification. For example, parts of the southwestern area were classified as low landslide susceptibility area despite the occurrence of multiple past landslides. Nonetheless, the SVM model showed good predictive performance, which was enhanced by the ACO and PSO algorithms.

In reality, predictive capability should not be regarded as the sole criterion for model selection. For LSM, the stability of the model is very critical. For example, the ACO-PSO-SVM model needs a relatively longer training time compared to the SVM model. Therefore, model selection is relatively subjective depending on the perspective of the user, planner, decision-maker, or even reader in specific circumstances. Besides, there is no doubt that the ACO-PSO-SVM model is an excellent tool for predicting landslide occurrence, and the results produced by the SVM model in this study are relatively acceptable. However, it is noticed that there remains the possibility of improving the SVM model's comprehensive performance. Therefore, novel optimization algorithms should be combined with the SVM to create more hybrid models for future work.

6. Discussion

The reliability and quality of LSM are influenced by conditioning factors, and certain factors may generate potential noise. Therefore, analyzing the relative contributions of factors to LSM can provide valuable guidance for landslide disaster management. However, due to the complexity of landslides, there is no global protocol or standard guideline for the selection of conditioning factors. The choice of conditioning factors is based on the availability of data relevant to the study area, the mechanism of landslide occurrences, and other similar landslide prediction studies. In the present study, IGR was used to assess the importance of the conditioning factors. Here, distance to faults, altitude, and slope angle were found to be the most important factors influencing the occurrence of landslides. The results of the IGR method showed that all the conditioning factors in the model had positive predictive capabilities. As such, all twelve conditioning factors were selected for the current landslide modeling.

The southeastern zone of the study area classified as having very high susceptibility is close to the fault. Due to the difference in physical and mechanical properties between the fault zone and bedrock, weathering and unloading are often formed in the fault zone, and the fault zone deforms slowly; as a result, the joints and fissures of the slope rock masses around the fault zone are densely developed. The mechanical properties of the damaged slope rock mass are reduced, and the stability of the slope becomes worse, so it is prone to landslide disasters, such as the Dagou landslide and the Zhongdaping landslide (Figure 11). Most of the landslides in the study area are located near the fault zone, and even many landslides are directly cut by faults (Figure 12). These phenomena confirm the correlation of fault proximity with landslide occurrence in the study area. In addition, in the southeastern region, lower altitudes have greater susceptibility than higher altitudes. The higher altitudes in the study area are mainly composed of resistant rock, but there might be a better explanation.

In recent years, various machine learning methods have been applied to domain-specific LSMs [51]. Although these methods have proven to be efficient in terms of prediction accuracy, until now, there is still no consensus on which method is best in LSM. The study of new methods is important to improve the performance of landslide susceptibility models. Ensemble-based hybrid machine learning methods are becoming increasingly popular in the assessment of landslide susceptibility due to their great advantages in terms of modeling and accuracy of output results. Generally, hybrid methods can result in more accurate and reliable susceptibility maps than those obtained using single simple models. For example, Hong et al. [52] proposed a hybrid fuzzy weight of the evidence model and obtained an AUC improvement of 0.025 over a single classifier. Pham et al. [29] demonstrated that the reduced error pruning tree model performed better when combined with hybrid machine learning approaches for LSM. Wang et al. [53] combined the stacking ensemble technique with three traditional machine learning methods (support vector machines, artificial neural networks, and gradient-boosting decision trees) to achieve an improved prediction of landslides. In this study, we designed and verified a novel hybrid model called ACO-PSO-SVM for the spatial prediction of landslide occurrence. Although the SVM model is one of the state-of-

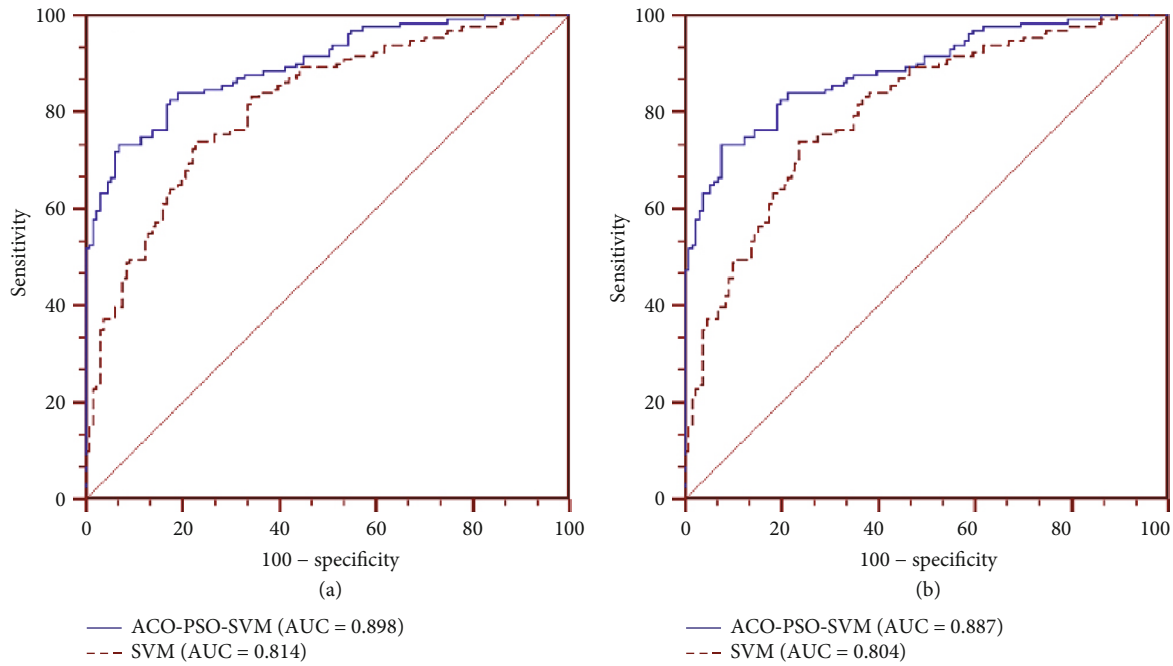

Figure 10: Comparison of the two models using the ROC curve technique: (a) success rate curve and (b) prediction rate curve.

Figure 11: Photographs of two landslides in the study area: (a) Dagou landslide; (b) Zhongdaping landslide.

the-art landslide modeling models with promising results, we tested the hypothesis that ACO and PSO ensemble learning techniques can significantly improve the predictive accuracy of SVM. The results show satisfactory agreement between the predicted susceptibility levels and the known landslide locations.

For the performance of the training dataset, the values of several statistical evaluation measures confirmed the superiority of the ACO-PSO-SVM model over the SVM model. For the PPV, the ACO-PSO-SVM model showed 88.0%, indicating that the probability of correctly classifying pixels in the training dataset as landslides is 88.0%. The highest NPV is for the ACO-PSO-SVM model (82.9%), which indicates that the probability of the model correctly classifying the pixels in the training dataset as nonlandslides is 82.9%. The ACO-PSO-SVM model had the best performance for the landslide location group (SST = 83.5%), indicating that 83.5% of the landslide pixels are correctly classified as landslides. The ACO-PSO-SVM model had the highest SPF value (87.6%), illustrating that 87.6% of the nonlandslide pixels are correctly classified as nonlandslides. In addition, the ACO-PSO-SVM model had the highest accuracy (85.4%) and kappa coefficient (0.756), indicating its excellent reliability and consistency. However, this does not determine which model is more predictive. Predictive power should be measured by the performance as determined by the validation dataset. Using the validation dataset, the results of all statistical evaluation measures confirmed that the ACO-PSO-

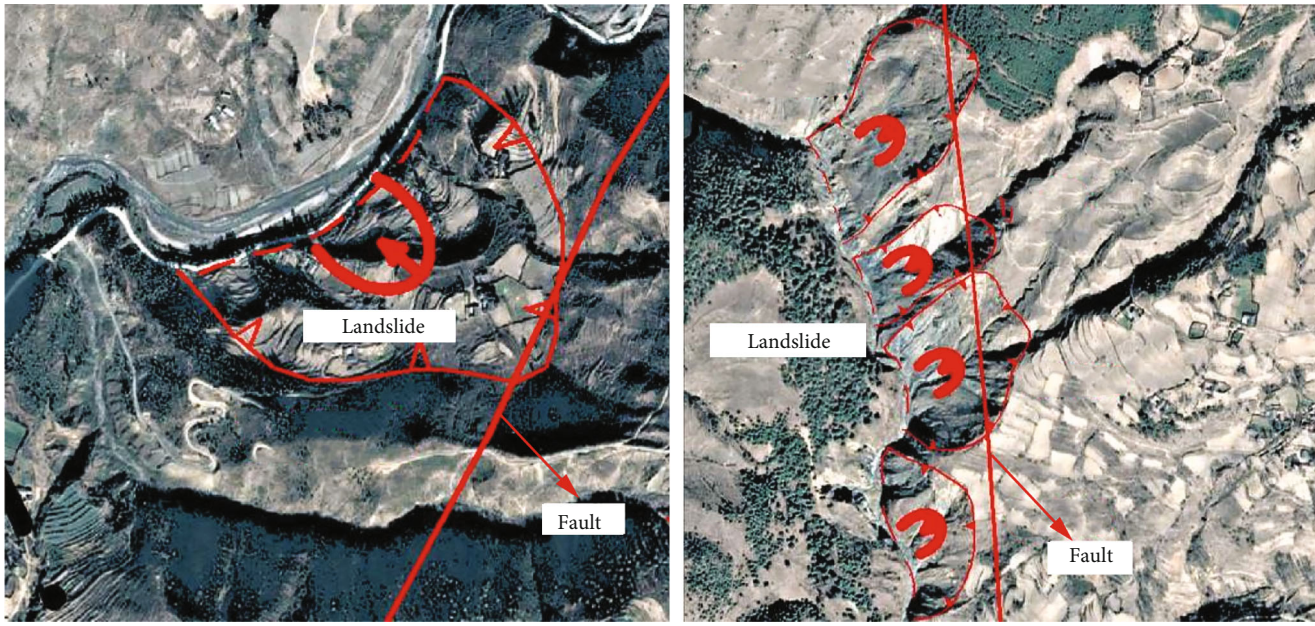

(a) (b)

Figure 12: Remote sensing images showing the fault observed at the rear edge of the landslide.

SVM model (PPV = 0.862, NPV = 0.826, SST = 0.831, SPF = 0.858, ACC = 0.844, and $\kappa = 0.743$) performed best. When using the hybrid framework, the SVM method improved by 7.90%, 7.90%, 7.60%, 8.3%, 7.90%, and 0.202 with respect to PPV, NPV, SST, SPF, ACC, and κ, respectively, and the hybrid method was more accurate than SVM with respect to the different evaluation measures. Overall, the two susceptibility models performed well in the classification of both landslide and nonlandslide pixels.

The AUC values between 0.7 and 0.9 imply a reasonable predictive capability [54]. The results confirm the highest performance and predictive capability of the ACO-PSO-SVM model for both the training (AUC = 0.898) and validation (AUC = 0.887) datasets. The corresponding values for SVM were lower (AUC training = 0.814; AUC validation = 0.804). By using the training and validation datasets, the ACO and PSO ensemble learning techniques improved the success and prediction rates of the SVM by 8.40% and 8.30%, respectively. The performance differences between the ACO-PSO-SVM model and the SVM model are related to ensemble learning leveraging the single methods and producing more reliable results. Overall, all two models showed reasonable prediction accuracy, with the highest one being for the ACO-PSO-SVM model. Therefore, the ACO-PSO-SVM model is considered the best model for LSM in this study. However, it is challenging to obtain the optimal model for LSM in a specific geo-environment among the countless models, and other hybrid models should be further explored.

7. Conclusions

The aim of this study was to analyze LSM through standalone and ensemble machine learning methods. For this purpose, twelve conditioning factors were extracted as key attributes for landslide occurrence, namely, altitude, slope angle, slope aspect, relief amplitude, cutting depth, gully density, SPI, lithology, rainfall, road density, distance to faults, and PGA. The IGR was used to evaluate the relative contribution of the conditioning factors. The performance of the hybrid model was then evaluated and compared to the single machine learning method using the ROC curve and several statistical measures. All twelve factors proposed in this study are more or less responsible for spatial landslide modeling, with distance to faults being the most important among them. The hybrid model based on ACO and PSO algorithms is a promising technique that can significantly enhance the performance of the solely applied model. In terms of overall performance, the ACO-PSO-SVM model is the best performing model for this study. The hybrid model produced the highest quality landslide susceptibility map, which is valuable for land-use planning and decision-making in landslide-prone areas.

Although this study has some contributions to LSM, there are some inherent limitations. The use of historical landslide inventories as input data is the main limitation of this paper. Due to limitations in the available images, resources, time, and cloud cover, we did not consider whether the data used were static landslides or earthquake-induced landslides. If the landslides triggered by an earthquake are not eliminated from the historical inventory, these landslides will introduce mapping errors in LSM. In the case of nonearthquake-induced landslides, the PGA as a conditioning factor was considered to provide an estimation of landslide susceptibility. In addition, the impact of different DEM spatial resolutions and the spatial heterogeneity of the landslide data on the evaluation results are ignored. In the future, we will separately study the LSM for the static landslides and earthquake-triggered landslides. Furthermore, how to couple the hybrid machine learning techniques for LSM still needs to be tested in different cases.

Data Availability

The data used in this manuscript have been included in the manuscript.

Conflicts of Interest

The authors declare that they have no known competing financial interests or personal relationships that could have appeared to influence the work reported in this paper.

Acknowledgments

The authors wish to thank the National Nature Science Foundation of China (No. 42107172), the Key Research Project of Sichuan Province (No. 2022YFN0023), the Fundamental Research Funds for the Sichuan University (No. 2021SCU12035), and the National Key R&D Program of China (No. 2018YFC1505004).

References

[1] Z. Chen, S. Liang, Y. Ke, Z. Yang, and H. Zhao, "Landslide susceptibility assessment using different slope units based on the evidential belief function model," *Geocarto International*, vol. 35, no. 15, pp. 1641–1664, 2020.

[2] K. Khanna, T. R. Martha, P. Roy, and K. V. Kumar, "Effect of time and space partitioning strategies of samples on regional landslide susceptibility modelling," *Landslides*, vol. 18, no. 6, pp. 2281–2294, 2021.

[3] D. M. Cruden and D. J. Varnes, "Landslide types and processes," *Landslides-Invesitgation and Mitigation*, vol. 247, pp. 36–75, 1996.

[4] G. Elia, F. Cotecchia, G. Pedone et al., "Numerical modelling of slope-vegetation-atmosphere interaction: an overview," *Quarterly Journal of Engineering Geology & Hydrogeology*, vol. 50, no. 3, pp. 249–270, 2017.

[5] G. Elia, G. Falcone, F. Cotecchia, and M. Rouainia, "Analysis of the effects of seasonal pore pressure variations on the slope stability through advanced numerical modelling," in *CNRIG 2019: Geotechnical Research for Land Protection and Development*, vol. 18, pp. 184–194, Springer, 2020.

[6] D. K. Keefer, "Landslides caused by earthquakes," *Geological Society of America Bulletin*, vol. 95, no. 4, p. 406, 1984.

[7] H. Tanyas, M. Rossi, M. Alvioli, C. J. van Westen, and I. Marchesini, "A global slope unit-based method for the near real-time prediction of earthquake-induced landslides," *Geomorphology*, vol. 327, pp. 126–146, 2019.

[8] F. Cotecchia, F. Santaloia, P. Lollino, C. Vitone, G. Pedone, and O. Bottiglieri, "From a phenomenological to a geomechanical approach to landslide hazard analysis," *European Journal of Environmental and Civil Engineering*, vol. 20, no. 9, pp. 1004–1031, 2016.

[9] F. Mori, A. Gena, A. Mendicelli, G. Naso, and D. Spina, "Seismic emergency system evaluation: the role of seismic hazard and local effects," *Engineering Geology*, vol. 270, p. 105587, 2020.

[10] P. Reichenbach, M. Rossi, B. D. Malamud, M. Mihir, and F. Guzzetti, "A review of statistically-based landslide susceptibility models," *Earth-Science Reviews*, vol. 180, pp. 60–91, 2018.

[11] X. Zhao and W. Chen, "Optimization of computational intelligence models for landslide susceptibility evaluation," *Remote Sensing*, vol. 12, no. 14, p. 2180, 2020.

[12] Y. Yang, J. Yang, C. Xu, C. Xu, and C. Song, "Local-scale landslide susceptibility mapping using the B-GeoSVC model," *Landslides*, vol. 16, no. 7, pp. 1301–1312, 2019.

[13] Z. Chen, F. Ye, W. Fu, Y. Ke, and H. Hong, "The influence of DEM spatial resolution on landslide susceptibility mapping in the Baxie River basin, NW China," *Natural Hazards*, vol. 101, no. 3, pp. 853–877, 2020.

[14] A. Aditian, T. Kubota, and Y. Shinohara, "Comparison of GIS-based landslide susceptibility models using frequency ratio, logistic regression, and artificial neural network in a tertiary region of Ambon, Indonesia," *Geomorphology*, vol. 318, pp. 101–111, 2018.

[15] S. Mondal and S. Mandal, "Data-driven evidential belief function (EBF) model in exploring landslide susceptibility zones for the Darjeeling Himalaya, India," *Geocarto International*, vol. 35, no. 8, pp. 818–856, 2020.

[16] P. Tsangaratos, I. Ilia, H. Hong, W. Chen, and C. Xu, "Applying information theory and GIS-based quantitative methods to produce landslide susceptibility maps in Nancheng County, China," *Landslides*, vol. 14, no. 3, pp. 1091–1111, 2017.

[17] W. Chen, X. Yan, Z. Zhao, H. Hong, D. T. Bui, and B. Pradhan, "Spatial prediction of landslide susceptibility using data mining-based kernel logistic regression, naive Bayes and RBF network models for the Long County area (China)," *Bulletin of Engineering Geology and the Environment*, vol. 78, no. 1, pp. 247–266, 2019.

[18] A. A. Shahri, J. Spross, F. Johansson, and S. Larsson, "Landslide susceptibility hazard map in Southwest Sweden using artificial neural network," *Catena*, vol. 183, p. 104225, 2019.

[19] J. Dou, A. P. Yunus, D. T. Bui et al., "Improved landslide assessment using support vector machine with bagging, boosting, and stacking ensemble machine learning framework in a mountainous watershed, Japan," *Landslides*, vol. 17, no. 3, pp. 641–658, 2020.

[20] W. Chen, S. Zhang, R. Li, and H. Shahabi, "Performance evaluation of the GIS-based data mining techniques of best-first decision tree, random forest, and naive Bayes tree for landslide susceptibility modeling," *Science of The Total Environment*, vol. 644, pp. 1006–1018, 2018.

[21] M. Panahi, A. Gayen, H. R. Pourghasemi, F. Rezaie, and S. Lee, "Spatial prediction of landslide susceptibility using hybrid support vector regression (SVR) and the adaptive neuro-fuzzy inference system (ANFIS) with various metaheuristic algorithms," *Science of The Total Environment*, vol. 741, p. 139937, 2020.

[22] S. Lee, M. J. Lee, H. S. Jung, and S. Lee, "Landslide susceptibility mapping using naïve bayes and bayesian network models in Umyeonsan, Korea," *Geocarto International*, vol. 35, no. 15, pp. 1665–1679, 2020.

[23] Y. Huang and L. Zhao, "Review on landslide susceptibility mapping using support vector machines," *Catena*, vol. 165, pp. 520–529, 2018.

[24] V. K. Pandey, H. R. Pourghasemi, and M. C. Sharma, "Landslide susceptibility mapping using maximum entropy and support vector machine models along the highway corridor, Garhwal Himalaya," *Geocarto International*, vol. 35, no. 2, pp. 168–187, 2020.

[25] W. Chen, M. Panahi, and H. R. Pourghasemi, "Performance evaluation of GIS-based new ensemble data mining techniques of adaptive neuro-fuzzy inference system (ANFIS) with genetic algorithm (GA), differential evolution (DE), and particle swarm optimization (PSO) for landslide spatial modelling," *Catena*, vol. 157, pp. 310–324, 2017.

[26] A. Jaafari, M. Panahi, B. T. Pham et al., "Meta optimization of an adaptive neuro-fuzzy inference system with grey wolf optimizer and biogeography-based optimization algorithms for spatial prediction of landslide susceptibility," *Catena*, vol. 175, pp. 430–445, 2019.

[27] S. V. Razavi-Termeh, K. Shirani, and M. Pasandi, "Mapping of landslide susceptibility using the combination of neuro-fuzzy inference system (ANFIS), ant colony (ANFIS-ACOR), and differential evolution (ANFIS-DE) models," *Bulletin of Engineering Geology and the Environment*, vol. 80, no. 3, pp. 2045–2067, 2021.

[28] D. T. Bui, P. Tsangaratos, V. T. Nguyen, N. Van Liem, and P. T. Trinh, "Comparing the prediction performance of a deep learning neural network model with conventional machine learning models in landslide susceptibility assessment," *Catena*, vol. 188, p. 104426, 2020.

[29] B. T. Pham, I. Prakash, S. K. Singh, A. Shirzadi, H. Shahabi, and D. T. Bui, "Landslide susceptibility modeling using reduced error pruning trees and different ensemble techniques: hybrid machine learning approaches," *Catena*, vol. 175, pp. 203–218, 2019.

[30] W. Chen and Y. Li, "GIS-based evaluation of landslide susceptibility using hybrid computational intelligence models," *Catena*, vol. 195, article 104777, 2020.

[31] M. I. Sameen, R. Sarkar, B. Pradhan, D. Drukpa, A. M. Alamri, and H. J. Park, "Landslide spatial modelling using unsupervised factor optimisation and regularised greedy forests," *Computational Geosciences*, vol. 134, p. 104336, 2020.

[32] H. F. Zhou, B. Liu, F. Ye, W. X. Fu, W. Q. Tang, and T. Fang, "Landslide distribution and sliding mode control along the Anninghe fault zone at the eastern edge of the Tibetan Plateau," *Journal of Mountain Science*, vol. 18, no. 8, pp. 2094–2107, 2021.

[33] A. Brenning, M. Schwinn, A. P. Ruiz-Páez, and J. Muenchow, "Landslide susceptibility near highways is increased by 1 order of magnitude in the Andes of southern Ecuador, Loja Province," *Natural Hazards and Earth System Sciences*, vol. 15, no. 1, pp. 45–57, 2015.

[34] P. Lollino, F. Cotecchia, G. Elia, G. Mitaritonna, and F. Santaloia, "Interpretation of landslide mechanisms based on numerical modelling: two case-histories," *European Journal of Environmental and Civil Engineering*, vol. 20, no. 9, pp. 1032–1053, 2016.

[35] M. A. Nowicki Jessee, M. W. Hamburger, K. Allstadt et al., "A global empirical model for near-real-time assessment of seismically induced landslides," *Journal of Geophysical Research - Earth Surface*, vol. 123, no. 8, pp. 1835–1859, 2018.

[36] J. Dou, A. P. Yunus, D. T. Bui et al., "Assessment of advanced random forest and decision tree algorithms for modeling rainfall-induced landslide susceptibility in the Izu-Oshima Volcanic Island, Japan," *Science of the Total Environment*, vol. 662, pp. 332–346, 2019.

[37] Y. Wu, Y. Ke, Z. Chen, S. Liang, H. Zhao, and H. Hong, "Application of alternating decision tree with AdaBoost and bagging ensembles for landslide susceptibility mapping," *Catena*, vol. 187, article 104396, 2020.

[38] J. Xie, T. Uchimura, P. Chen, J. Liu, C. Xie, and Q. Shen, "A relationship between displacement and tilting angle of the slope surface in shallow landslides," *Landslides*, vol. 16, no. 6, pp. 1243–1251, 2019.

[39] N. B. Raja, I. Çiçek, N. Türkoğlu, O. Aydin, and A. Kawasaki, "Landslide susceptibility mapping of the Sera River Basin using logistic regression model," *Natural Hazards*, vol. 85, no. 3, pp. 1323–1346, 2017.

[40] M. Abedini, B. Ghasemian, A. Shirzadi et al., "A novel hybrid approach of bayesian logistic regression and its ensembles for landslide susceptibility assessment," *Geocarto International*, vol. 34, no. 13, pp. 1427–1457, 2019.

[41] Y. Yi, Z. Zhang, W. Zhang, Q. Xu, C. Deng, and Q. Li, "GIS-based earthquake-triggered-landslide susceptibility mapping with an integrated weighted index model in Jiuzhaigou region of Sichuan Province, China," *Natural Hazards and Earth System Sciences*, vol. 19, no. 9, pp. 1973–1988, 2019.

[42] J. Dou, K. T. Chang, S. Chen et al., "Automatic case-based reasoning approach for landslide detection: integration of object-oriented image analysis and a genetic algorithm," *Remote Sensing*, vol. 7, no. 4, pp. 4318–4342, 2015.

[43] H. Chen, H. Liu, J. Han, X. Yin, and J. He, "Exploring optimization of semantic relationship graph for multi-relational Bayesian classification," *Decision Support Systems*, vol. 48, no. 1, pp. 112–121, 2009.

[44] K. Chapi, V. P. Singh, A. Shirzadi et al., "A novel hybrid artificial intelligence approach for flood susceptibility assessment," *Environmental Modelling & Software*, vol. 95, pp. 229–245, 2017.

[45] B. T. Pham, D. T. Bui, H. R. Pourghasemi, P. Indra, and M. B. Dholakia, "Landslide susceptibility assesssment in the Uttarakhand area (India) using GIS: a comparison study of prediction capability of naïve Bayes, multilayer perceptron neural networks, and functional trees methods," *Theoretical and Applied Climatology*, vol. 128, no. 1-2, pp. 255–273, 2017.

[46] A. R. Adly, S. H. A. Aleem, M. A. Algabalawy, F. Jurado, and Z. M. Ali, "A novel protection scheme for multi-terminal transmission lines based on wavelet transform," *Electric Power Systems Research*, vol. 183, pp. 106286–106286, 2020.

[47] M. Dorigo and L. M. Gambardella, "Ant colony system: a cooperative learning approach to the traveling salesman problem," *IEEE Transactions on Evolutionary Computation*, vol. 1, no. 1, pp. 53–66, 1997.

[48] X. Zhang, H. Liu, and L. Tu, "A modified particle swarm optimization for multimodal multi-objective optimization," *Applied Artificial Intelligence*, vol. 95, p. 103905, 2020.

[49] V. N. Vapnik, "An overview of statistical learning theory," *IEEE Transactions on Neural Networks*, vol. 10, no. 5, pp. 988–999, 1999.

[50] B. T. Pham, T. A. Hoang, D. M. Nguyen, and D. T. Bui, "Prediction of shear strength of soft soil using machine learning methods," *Catena*, vol. 166, pp. 181–191, 2018.

[51] A. Arabameri, S. Saha, J. Roy, W. Chen, T. Blaschke, and D. Tien Bui, "Landslide susceptibility evaluation and management using different machine learning methods in the Gallicash River Watershed, Iran," *Remote Sensing*, vol. 12, no. 3, p. 475, 2020.

[52] H. Hong, I. Ilia, P. Tsangaratos, W. Chen, and C. Xu, "A hybrid fuzzy weight of evidence method in landslide susceptibility analysis on the Wuyuan area, China," *Geomorphology*, vol. 290, pp. 1–16, 2017.

[53] Y. Wang, L. Feng, S. Li, F. Ren, and Q. Du, "A hybrid model considering spatial heterogeneity for landslide susceptibility mapping in Zhejiang Province, China," *Catena*, vol. 188, p. 104425, 2020.

[54] T. Fawcett, "An introduction to ROC analysis," *Pattern Recognition Letters*, vol. 27, no. 8, pp. 861–874, 2006.